




# On the measurement of effective powder layer thickness in laser powder-bed fusion additive manufacturing of metals

Yahya Mahmoodkhani<sup>1</sup> · Usman Ali<sup>1</sup> · Shahriar Imani Shahabad<sup>1</sup> · Adhitan Rani Kasinathan<sup>1</sup> · Reza Esmaeilizadeh<sup>1</sup> · Ali Keshavarzkermani<sup>1</sup> · Ehsan Marzbanrad<sup>1</sup> · Ehsan Toyserkani<sup>1</sup> 

Received: 10 June 2018 / Accepted: 14 August 2018 / Published online: 21 August 2018  
© Springer Nature Switzerland AG 2018

## Abstract

In laser powder-bed fusion (LPBF), the actual thickness of powder particles that spread on solidified zones, so-called effective layer thickness (ELT), is higher than the nominal layer thickness. The source cause of this discrepancy is the fact that powder particles substantially shrink after selective melting, followed by solidification. ELT, as an unknown parameter, depends on process parameters and material properties. In this study, an effective method to measure ELT is proposed and applied to 17-4 PH stainless steel for a nominal build layer thickness of 20  $\mu\text{m}$ . The measured ELT was larger than 100  $\mu\text{m}$ , which is far beyond the values reported in the literature. Results obtained from the current study show the effect of applying the ELT rather than the nominal build layer thickness in numerical modeling studies as well as understanding the governing physics in the LPBF process.

**Keywords** Additive manufacturing · Laser–powder bed fusion · Effective layer thickness

## 1 Introduction

During laser powder-bed fusion (LPBF), powder characteristics directly govern the final part properties. For example, the layer thickness is directly related to the part density [1, 2]. In addition, the powder flowability, size distribution, etc. affect the final part properties and, therefore, play an important role to achieve high-quality parts [1, 3, 4]. On the other hand, better understanding of powder characteristics such as powder bed density and powder layer thickness helps in defining proper boundary conditions for computer modeling of the LPBF process.

In LPBF, the powder bed characteristics and laser–powder interaction define the most critical aspects of the process. Several studies in the literature have identified layer thickness as one of the most important parameters in LPBF [2, 5, 6]. Layer thickness is identified as the new layer of powder spread on top of the previously solidified zone. One

should, however, differentiate the nominal layer thickness and actual layer thickness referred to as the effective layer thickness (ELT). Theoretically, ELT is assumed to be larger than the nominal build layer thickness due to the shrinkage after melting and solidification.

There are several theoretical estimations of ELT in the literature [5, 7, 8], where ELT is considered to be around double the build layer thickness. Spierings et al. [5] assumed a powder layer density of 60% to estimate ELT while Mindt et al. [9] assumed a packing density of 50% to calculate ELT. Similarly, Zhang et al. [7] and Gurtler et al. [8] proposed a mathematical model to calculate ELT. A wide range of 38–60% relative powder bed compaction density is reported in laser powder-bed fusion [10]. Although efforts have been made to determine the relative compaction density of powder bed using experimental and simulation tools and correlate it to ELT [11–13], the literature lacks a systematic experimental study to determine the accurate value of ELT.

In this paper, a method for the accurate measurement of ELT during LPBF is proposed. The measured values are then validated through profilometry data using a confocal microscope. To the best knowledge of the authors, this is the first work that presents a methodology to efficiently measure ELT. As layer thickness is an input for numerical modeling of LPBF, an accurate measurement of ELT is of importance

✉ Ehsan Toyserkani  
ehsan.toyserkani@uwaterloo.ca

<sup>1</sup> Multi-Scale Additive Manufacturing Lab, Department of Mechanical and Mechatronics Engineering, University of Waterloo, 200 University Avenue West, Waterloo, ON N2L 3G1, Canada

as it directly affects the calculated temperature distribution, melt pool geometry, residual stresses, etc.

## 2 Experimental

### 2.1 Material and additive manufacturing setup

A commercially available Stainless Steel SS17-4 PH powder from EOS GmbH (Krailling, Germany) was used in this study with D10, D50, and D90 of 30.2  $\mu\text{m}$ , 42.4  $\mu\text{m}$ , 58.1  $\mu\text{m}$ . An EOS M290 (EOS GmbH, Krailling, Germany) was used to build the LPBF samples. A nominal build layer thickness of 20  $\mu\text{m}$  was used for printing all LPBF parts. Parameter values for laser speed, laser power, and hatching distance were set to be 1108 mm/s, 227 W and 90  $\mu\text{m}$ , respectively.

### 2.2 Characterization

A Retsch Camsizer X2 (Retsch Technology GmbH, Haan, Germany) was used to measure the powder size distribution and a Keyence VK-X250 (Keyence Corporation, Osaka, Japan) confocal microscope was used to measure the surface topology and dimensions of the LPBF samples.

### 2.3 Procedure for effective layer thickness measurement

To achieve a representative data set, nine parts with a cross section of 4 mm  $\times$  6 mm (Fig. 1b) and 4 mm height were printed at various locations on the substrate (Fig. 1a). The substrate was divided into nine regions with parts printed at the center of each region as shown in Fig. 1a. Parts were made with thin walls (Fig. 1b) parallel to the recoater moving direction. Each part had three slots with depths of 20  $\mu\text{m}$ ,

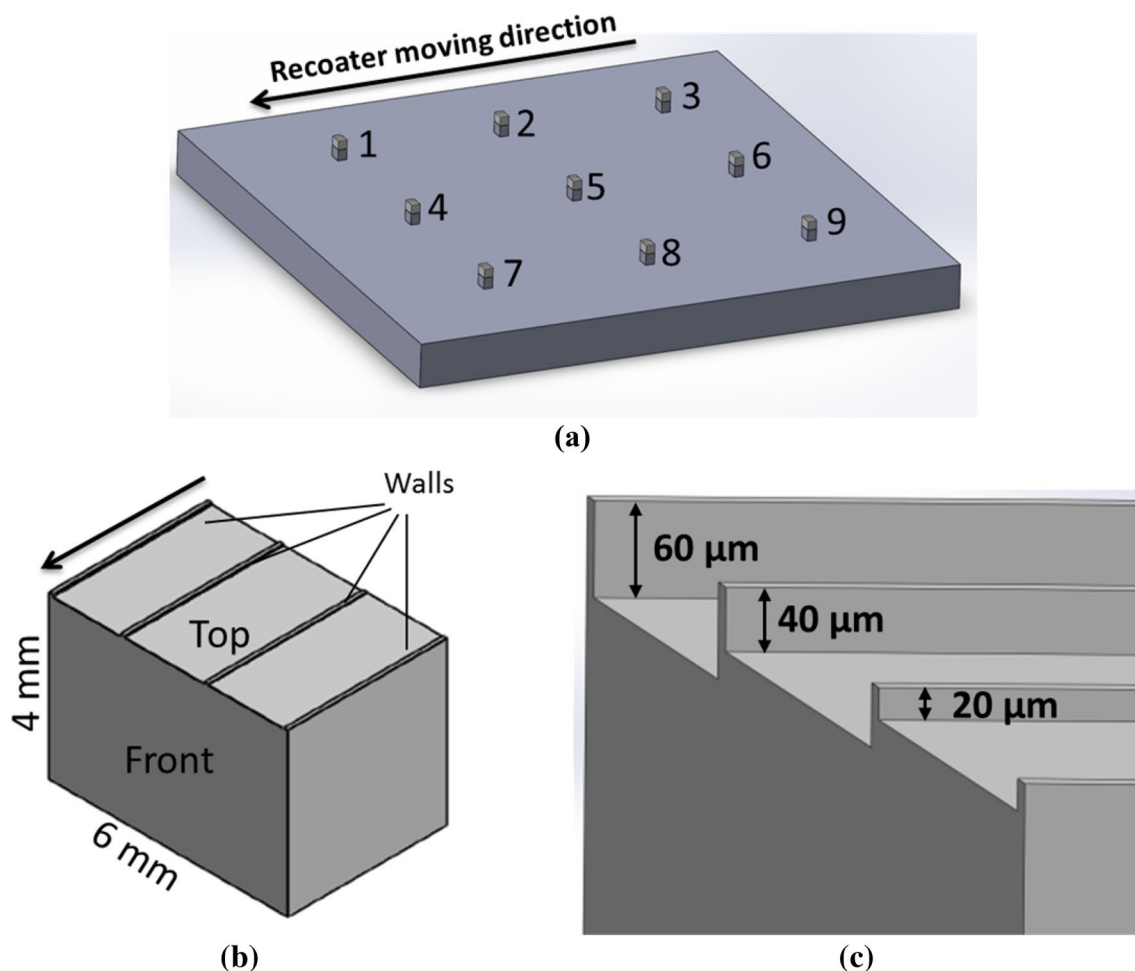


**Fig. 1** a Arrangement of stainless steel samples on the substrate, b, c geometry of the sample designed for measuring the effective powder layer thickness

40  $\mu\text{m}$  and 60  $\mu\text{m}$  as shown in Fig. 1c. These slots were made to validate the surface depth data measured by the confocal microscope. The height difference between adjacent slots (20  $\mu\text{m}$ ) was designed to confirm if the build layer thickness had reached a steady-state regime.

Procedure to measure the ELT is shown in Fig. 2. To print the thin walls (Fig. 1b), a new layer of powder was laid on top of the previously solidified part (Step 1). Next, the laser scanned the powder to print the thin walls. At this point, the printing is complete. Then, the recoater was moved towards the right to its original position as shown in Step 2 and then moved to left across the build compartment while the build plate was kept at the same height as the last recoating step so that it could scratch some areas on the printed walls (Step 3). The scratched areas resulted in flattened peaks that were used as reference points to measure the ELT. In addition, as the flatted peaks correspond to the height of the previous layer, the height difference between the peaks and the

surface of the sample would be equal to the effective layer thickness of powder on top of the build surface (Step 3). The 20- $\mu\text{m}$ , 40- $\mu\text{m}$  and 60- $\mu\text{m}$  steps on the samples (Fig. 1c) along with the reference height from scratched walls were used to measure the ELT during LPBF.

### 2.4 Numerical thermal model

Finite element (FE) simulations were performed to study the effect of ELT on the temperature change during the LPBF process. FE simulations using COMSOL Multiphysics® were performed to model temperature distribution and melt pool dimensions with layer thickness of 20 and 150  $\mu\text{m}$ . Laser exposure parameters such as speed and power were based on experimental values (laser speed, laser power, and hatching distance were set to be 1108 mm/s, 227 W and 90  $\mu\text{m}$ , respectively).

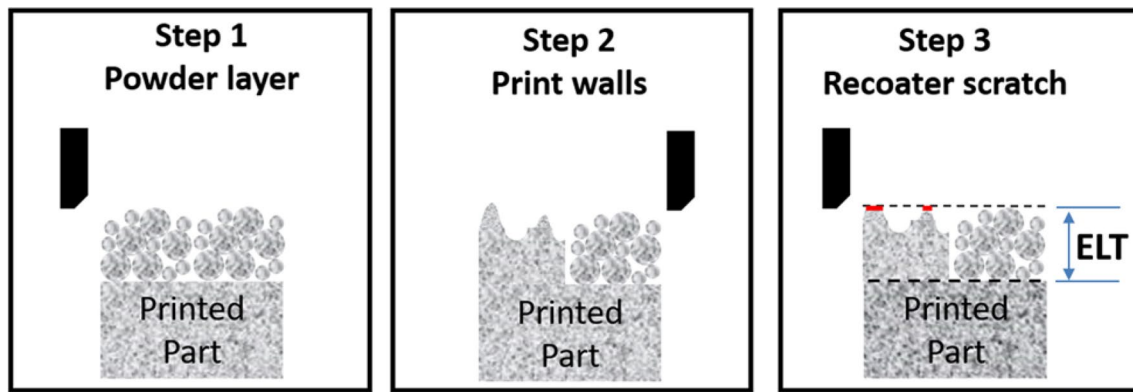
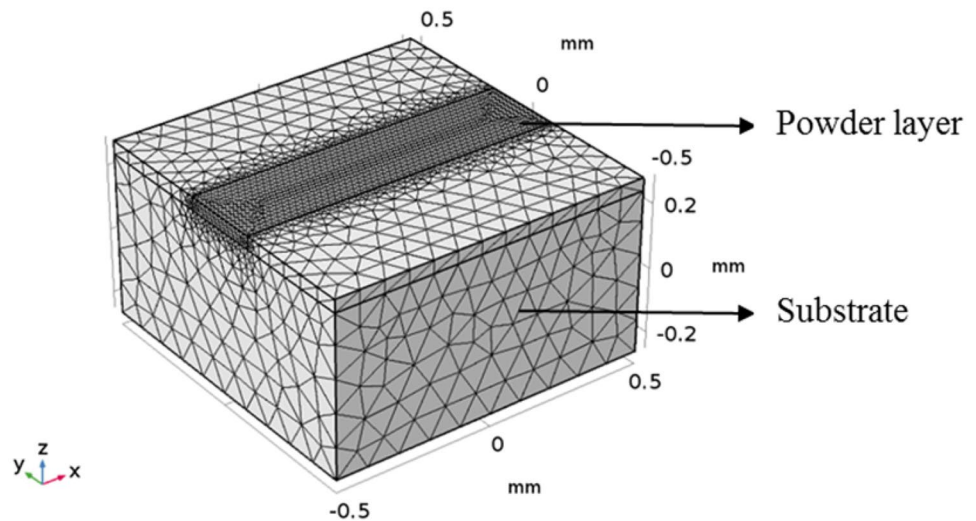


Fig. 2 Schematic showing the steps taken to measure effective powder layer thickness (ELT)

Table 1 Thermo-physical properties of SS17-4PH, powder and heat source parameters [14, 16]

Category	Parameter (unit)	Value
Bulk properties (at room temperature)	Density, $\rho$ ( $\text{kg}/\text{m}^3$ )	7740
	Heat conductivity, $k$ ( $\text{W}/\text{mK}$ )	11.5
	Specific heat, $C_p$ ( $\text{J}/\text{kgK}$ )	426
	Melting range (K)	1677–1713
	Latent heat ( $\text{KJ}/\text{kg}$ )	280
Powder parameters (at room temperature)	Powder porosity, $\varphi$	50%
	Calculated powder conductivity, $k$ ( $\text{W}/\text{mK}$ )	0.1419
	$k_s$ ( $\text{W}/\text{mK}$ )	11.5
	$k_g$ ( $\text{W}/\text{mK}$ )	0.018
	$\emptyset$	0.0003
	$B$	1
Heat source parameters	$Q_0$ ( $\text{W}/\text{m}^3$ )	5.685E14
	$r_e$ ( $\mu\text{m}$ )	50
	$r_i$ ( $\mu\text{m}$ )	30
	$Z_e - Z_i$ ( $\mu\text{m}$ )	180

**Fig. 3** Mesh size of the domain including powder layer and substrate



Governing equation (Fourier law of heat transfer) is described in Eqs. (1) and (2) where  $\rho$ ,  $C_p$ ,  $k$ ,  $u$ ,  $T$ ,  $q$  and  $Q$  are the density, specific heat, thermal conductivity, velocity field, temperature, heat flux density and volumetric heat source, respectively.

$$\rho C_p \frac{\partial T}{\partial t} + \rho C_p u \cdot \nabla T + \nabla \cdot q = Q, \tag{1}$$

$$q = -k \nabla T. \tag{2}$$

The effective thermal conductivity of powder bed is determined by the following equation [14]:

$$\frac{k}{k_g} = \left(1 - \sqrt{1 - \varphi}\right) \left(1 + \frac{\varphi k_R}{k_g}\right) + \sqrt{1 - \varphi} \left\{ (1 - \vartheta) \left[ \frac{2}{1 - \frac{B k_g}{k_s}} \left( \frac{B}{\left(1 - \frac{B k_g}{k_s}\right)^2} \left(1 - \frac{k_g}{k_s}\right) \text{Ln} \frac{k_s}{B k_g} - \frac{B + 1}{2} - \frac{B - 1}{1 - \frac{B k_g}{k_s}} \right) + \frac{k_R}{k_g} \right] + \vartheta \frac{k_{\text{Contact}}}{k_g} \right\}, \tag{3}$$

where  $k$  is effective thermal conductivity of powder bed,  $k_g$  is thermal conductivity of continuous gas phase,  $k_s$  is thermal conductivity of skeletal solid,  $\varphi$  is porosity of powder bed which is related to powder bed density,  $k_R$  is thermal conductivity part of the powder bed owing to radiation,  $\vartheta$  is flattened surface fraction of particle in contact with another particle,  $B$  is deformation parameter of the particle, and  $k_{\text{contact}}$  is conditionally calculated as following:

$$k_{\text{contact}} = 18 \vartheta k_s \quad \text{if } \vartheta < 3 \times 10^{-4},$$

$$k_{\text{contact}} \approx k_s \quad \text{if } \vartheta > 0.01.$$

The volumetric heat source  $Q$  is implemented as shown in the following equations [15]:

$$Q_v(r, z) = Q_0 \exp\left(-\frac{2r^2}{r_0^2}\right), \tag{4}$$

$$r_0(z) = r_e - (r_e - r_i) \frac{z_e - z}{z_e - z_i}, \tag{5}$$

where  $Q_0$  is the maximum heat intensity,  $r_0$  is the distribution parameter,  $z_e$  and  $z_i$  represent the top and bottom surfaces, respectively.

Table 1 lists the values of parameters used for the simulation.

In this work, to compensate the latent heat of fusion during melting, the specific heat of material was increased in

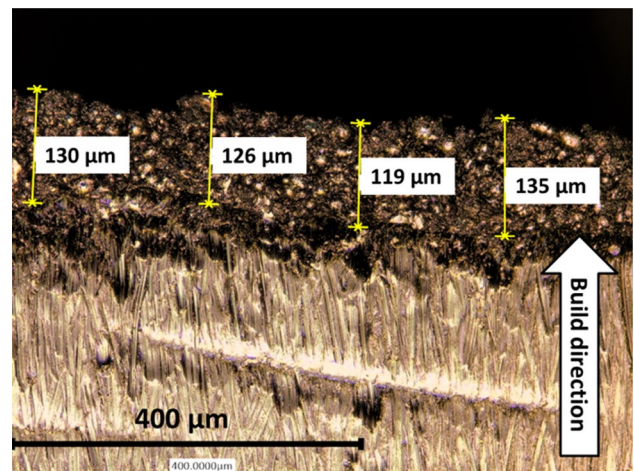


**Fig. 4** A single layer of powder adhered onto the printed part



the melting range so that the extra energy absorbed in the melting range becomes equal to the latent heat of fusion.

Figure 3 shows the meshed substrate and powder layer. Fine tetrahedral elements were implemented in powder layer region to account for the laser–powder interaction whereas a coarser mesh size was used for the substrate. In addition, the

bottom surface was set to an ambient temperature of 298 K. Heat transfer due to atmospheric convection was applied to all boundaries and radiative heat transfer was considered on the top surface.

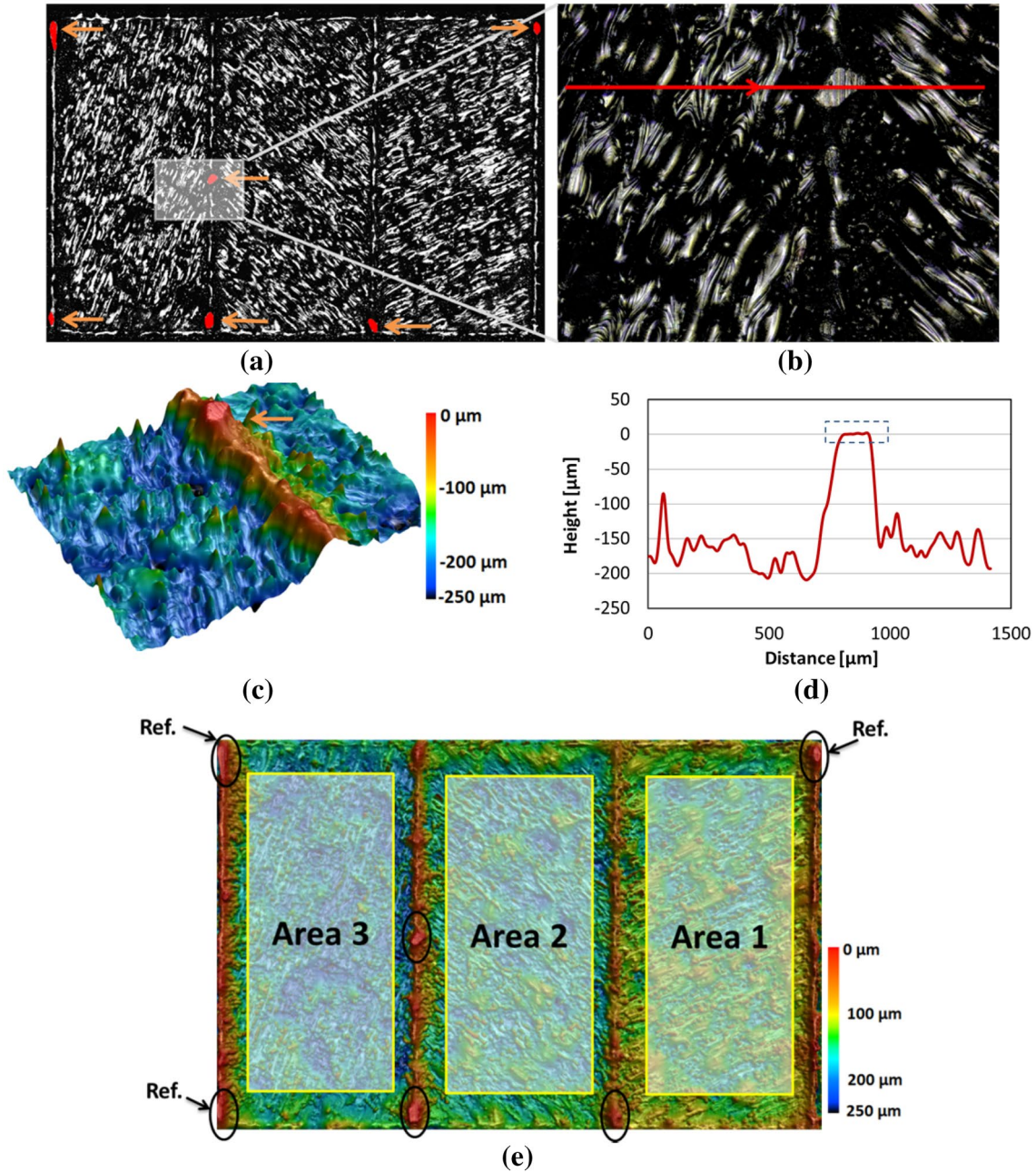


**Fig. 5** **a** Macrograph from flat regions on the supporting walls created due to recoater motion on Sample 1. **b** Zoomed area contacted by the recoater on Sample 1. **c** Surface topology for the highlighted

area in **a**. **d** Surface profile on the line shown in **b**. **e** Confocal microscope graph showing the surface profile of Sample 1

### 3 Results and discussion

#### 3.1 Experimental ELT measurements

Micrograph of a sample with a layer of the powder particles is shown in Fig. 4. This sample was made by gluing the powder particles on top of the printed part with droplets of Super Glue (a low-viscose liquid cyanoacrylate adhesive) and then cutting and polishing the section normal to the surface to measure ELT.

The method described in the previous section was applied to the nine samples printed on various areas of the substrate (Fig. 1a). Figure 5 demonstrates the measurement of ELT from the laser confocal microscopy results. Areas, where recoater made contact with the supporting walls on the sample surface, are highlighted in Fig. 5a. Flat regions represent the contact points with the recoater and hence the elevation of the powder for the last printed layer. Figure 5b, c shows the magnified 2D and 3D views of the highlighted region in Fig. 5a, respectively, and shows the flat surface produced by the recoater scratch on the supporting walls. Figure 5d represents the height profile of the horizontal red line shown in Fig. 5b. The dotted square in Fig. 5d highlights the scratched area of the supporting wall and shows the same height across the whole surface thus confirming the flatness of the area.

An example (Sample 1) is shown in Fig. 5e. It is noted that the average depth of areas 1, 2 and 3 shown in Fig. 5e is measured with respect to a plane passing through the reference points (Ref.) shown in Fig. 5e.

Surface contours for nine samples printed at different locations of the substrate are shown in Fig. 6. The measured values for the average depth of three areas on top of all nine samples are also written in the corresponding region in Fig. 6. The middle row samples (Samples 4, 5 and 6) show shallower surface indicating a thicker ELT for these samples and the top row (Samples 1, 2 and 3) shows relatively thinner ELT.

Table 2 shows the average measured values for all areas shown in Fig. 5e. The average depth of areas 1, 2 and 3 for each sample shows ELT for 20  $\mu\text{m}$ , 40  $\mu\text{m}$ , and 60  $\mu\text{m}$  steps, respectively. Results show that the average depth for Area 1 (20  $\mu\text{m}$  build layer thickness) is 153  $\mu\text{m}$  which is about an order of magnitude greater than the build layer thickness. It should be noted that even though ELT is about an order of magnitude greater than the build layer thickness, the effective height difference between 20- $\mu\text{m}$ , 40- $\mu\text{m}$ , and 60- $\mu\text{m}$  steps (Area 1, Area 2 and Area 3) is  $\sim 20$   $\mu\text{m}$ .

The relative step size of  $\sim 20$   $\mu\text{m}$  on the surface of the build confirms two facts: (1) the build layer thickness is in steady-state regime and equal to the nominal layer thickness of 20  $\mu\text{m}$

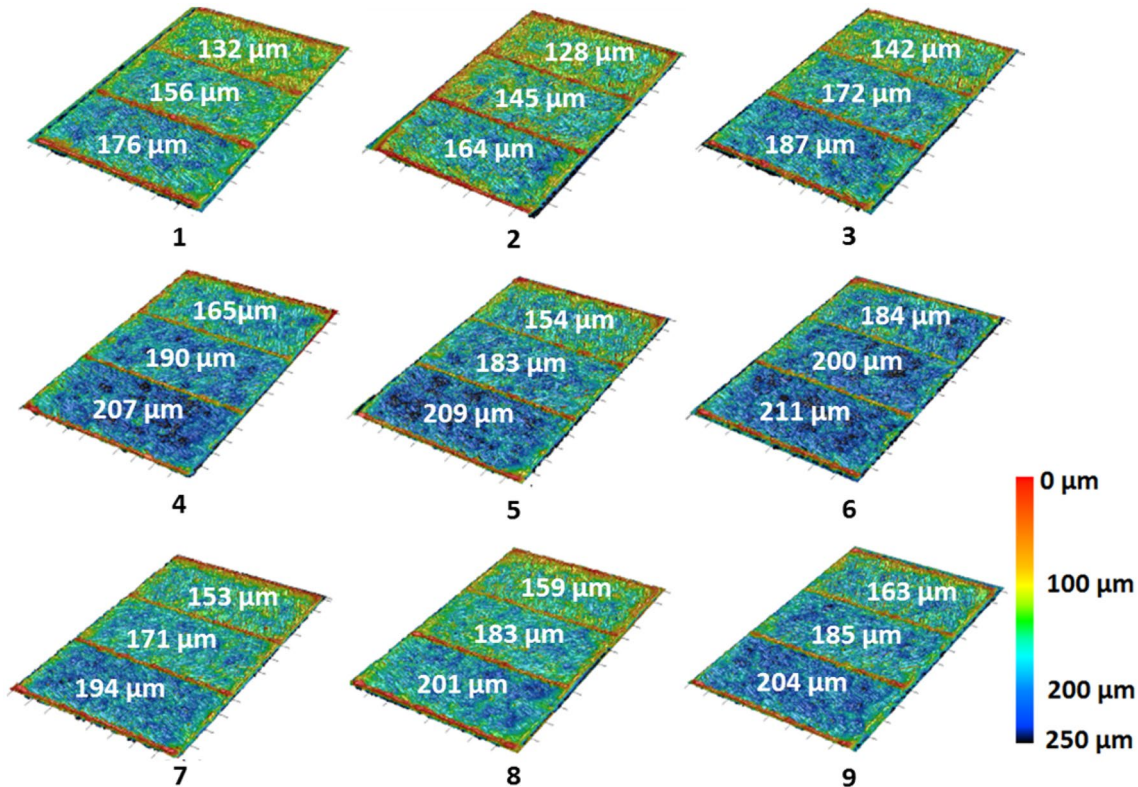


Fig. 6 Surface profile for the printed samples with the depth of each area with respect to the reference plane (ELT)

while an ELT of  $\sim 150 \mu\text{m}$  is maintained between the powder top surface and solidified zone during the production, and (2) it confirms the validity of measured values with the confocal microscope.

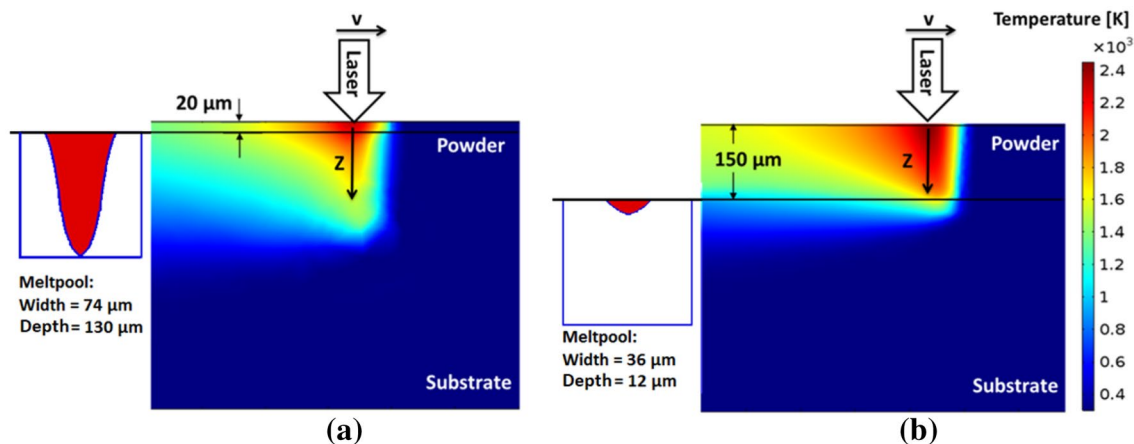
### 3.2 Effect of ELT on model-predicted temperatures

Experimental results presented in the previous section highlight the difference between ELT and nominal layer thickness. However, it is important to understand the effect of this difference, if any, on printed parts. Therefore, simulations with nominal layer thickness and ELT were performed to study the temperature and melt pool dimensions.

Predicted effects of the powder layer thickness on the temperature distribution during LPBF are shown in Fig. 7a, b. The same heat source parameters and boundary conditions were used for both simulations. Results in Fig. 7a, b show differences between the temperature profiles for nominal ( $20 \mu\text{m}$ ) and effective ( $150 \mu\text{m}$ ) powder layer thickness. Inserts in Fig. 7a, b show the melt pool shape and dimensions for the nominal and ELT. Simulated results for nominal and effective layer thickness show a huge difference between the melt pool depth ( $130$  and  $12 \mu\text{m}$ , respectively) and width ( $74$  and  $36 \mu\text{m}$ , respectively) that highlights the effect of ELT.

**Table 2** Measurements and statistical data of areas shown in Fig. 6 with respect to the reference plane for SS 17-4 PH samples shown in Fig. 1

Sample	Average depth ( $\mu\text{m}$ )			Relative height difference ( $\mu\text{m}$ )	
	Area 1	Area 2	Area 3	Area 1–Area 2	Area 2–Area 3
Average	153	176	195	22	19
SD	16.4	16.2	15.3	4.4	4.1



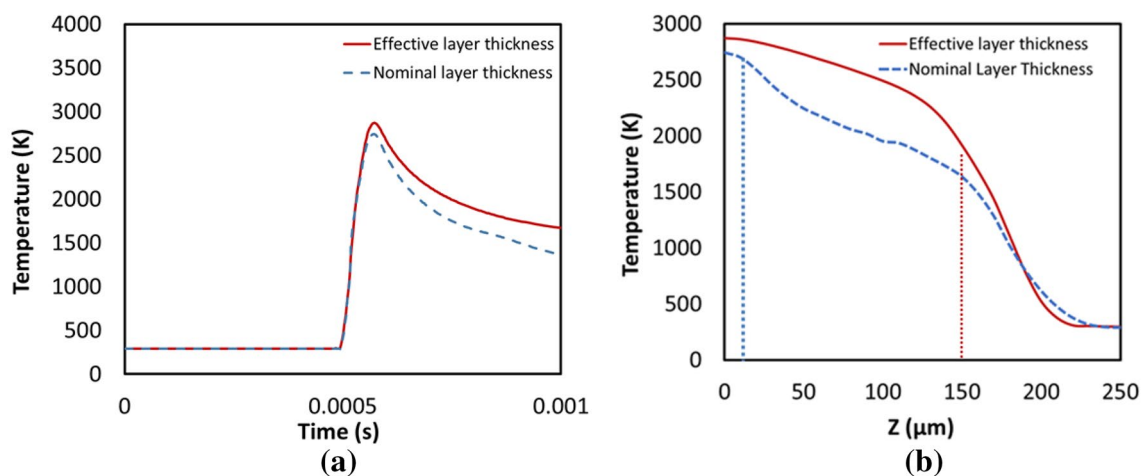
**Fig. 7** FE model-predicted temperature distribution in LPBF process with different powder layer thickness; **a** nominal layer thickness ( $20 \mu\text{m}$ ) and **b** effective layer thickness ( $150 \mu\text{m}$ ). Note: the inserts in **a**, **b** show the melt pool shape. The same process parameters were used for **a**, **b**

Figure 8a, b shows simulation results for the effect of powder layer thickness on temperature history (Fig. 8a) and the temperature profile from the free surface of the powder under the laser (Fig. 8b). The dotted lines in Fig. 8b show the beginning of substrate (previously solidified surfaces) corresponding to the nominal and effective layer thickness. These predictions show the effect of the powder layer thickness on the temperature distribution. Referring to Fig. 8a, ELT results show higher peak temperature. The powder layer offers less conductivity than solid material; therefore, the heat transferred to the previously solidified material under effective powder layer is much less than the nominal layer. This is also seen clearly in the temperature at the substrate surface under nominal ( $\sim 2700 \text{ K}$ ) and effective ( $\sim 1850 \text{ K}$ ) powder layers (Fig. 8b).

### 4 Conclusion

In this paper, a novel method to measure the thickness of powder over the previously solidified material, also known as the effective layer thickness (ELT), was presented. In contrast to studies and simulations on powder compaction and ELT in LPBF, findings of this research show that ELT ( $153 \mu\text{m}$ ) is about an order of magnitude larger than the build layer thickness ( $20 \mu\text{m}$ ) for 17-4 PH stainless steel for the input process parameters used in this paper. As ELT is much larger than the nominal layer thickness, simulated results show a pronounced effect on the temperature distribution (up to  $120 \text{ }^\circ\text{C}$  under prediction) and melt pool dimensions (up to ten times overprediction) during LPBF.





**Fig. 8** **a** Model-predicted temperature history at the surface of powder for two different powder layer thicknesses (the points are shown in Fig. 7) and **b** temperature profile in depth under the laser ( $z$ -direction in Fig. 7)

**Acknowledgements** This work was supported by funding from the Natural Sciences and Engineering Research Council of Canada (NSERC) and the Federal Economic Development Agency for Southern Ontario (FedDev Ontario). The authors would also like to acknowledge the help from Jerry Rathapakdee and Karl Rautenberg for helping with design and printing the LPBF parts.

## References

- Fayazfar H et al (2018) A critical review of powder-based additive manufacturing of ferrous alloys: process parameters, microstructure and mechanical properties. *Mater Des* 144:98–128
- Ma M, Wang Z, Gao M, Zeng X (2015) Layer thickness dependence of performance in high-power selective laser melting of 1Cr18Ni9Ti stainless steel. *J Mater Process Technol* 215(1):142–150
- Spierings AB, Herres N, Levy G (2011) Influence of the particle size distribution on surface quality and mechanical properties in AM steel parts. *Rapid Prototyp J* 17(3):195–202
- Tan JH, Wong WLE, Dalgarno KW (2017) An overview of powder granulometry on feedstock and part performance in the selective laser melting process. *Addit Manuf* 18:228–255
- Spierings AB, Levy G (2009) Comparison of density of stainless steel 316L parts produced with selective laser melting using different powder grades. In: *Solid Free. Fabr. Proc.*, pp 342–353
- Meier H, Haberland C (2008) Experimental studies on selective laser melting of metallic parts. *Materwiss Werkstsch* 39(9):665–670
- Zhang DQ, Cai QZ, Liu JH, Li RD (2010) A powder shrinkage model for describing real layer thickness during selective laser melting process. *Adv Mater Res* 97–101:3820–3823
- Gürtler Fj, Karg M, Dobler M, Kohl S, Tzivilsky I, Schmidt M (2014) Influence of powder distribution on process stability in laser beam melting: Analysis of melt pool dynamics by numerical simulations. In: *Solid free. symp. Texas*, pp 1099–1117
- Mindt HW, Megahed M, Lavery NP, Holmes MA, Brown SGR (2016) Powder bed layer characteristics: the overseen first-order process input. *Metall Mater Trans A Phys Metall Mater Sci* 47(8):3811–3822
- Ali U et al (2018) On the measurement of relative On the measurement of relative powder-bed compaction density in powder-bed additive manufacturing processes. *J Mater Des* 155:495–501
- Jacob G, Donmez A, Slotwinski J, Moylan S (2016) Measurement of powder bed density in powder bed fusion additive manufacturing processes. *Meas Sci Technol* 27(11):115601
- Egger G, Gygax PE, Glardon R, Karapatis NP (1999) Optimization of powder layer density in selective laser sintering. In: *10th Solid Free. Fabr. Symp.*, pp 255–263
- Choi J-P et al (2017) Evaluation of powder layer density for the selective laser melting (SLM) process. *Mater Trans* 58(2):294–297
- Kundakcioglu E, Lazoglu I, Poyraz Ö, Yasa E, Cizicioğlu N (2018) Thermal and molten pool model in selective laser melting process of Inconel 625. *Int J Adv Manuf Technol* 95:3977–3984
- Martinson P, Daneshpour S, Koçak M, Riekehr S, Staron P (2009) Residual stress analysis of laser spot welding of steel sheets. *Mater Des* 30(9):3351–3359
- Sabau AS, Porter WD (2008) Alloy shrinkage factors for the investment casting of 17-4PH stainless steel parts. *Metall Mater Trans B Process Metall Mater Process Sci* 39(2):317–330

**Publisher's Note** Springer Nature remains neutral with regard to jurisdictional claims in published maps and institutional affiliations.